International Journal of Nanomedicine

Dovepress
Taylor & Francis Group

Open Access Full Text Article

ORIGINAL RESEARCH

In situ Antibiotic-Loaded Copper Tannic Acid Coordination Nanospheres Targeting Biofilms for the Treatment of Chronic Osteomyelitis

Ziming Ren[1,*], Yuelei Zhang[1,*], Yanyan Liu[2,3], Gang Wang[1]

[1]Department of Traumatic Orthopedics, The First Affiliated Hospital of Anhui Medical University, Hefei, Anhui, People's Republic of China; [2]Department of Infectious Diseases & Anhui Center for Surveillance of Bacterial Resistance, The First Affiliated Hospital of Anhui Medical University, Hefei, Anhui, People's Republic of China; [3]Anhui Province Key Laboratory of Infectious Diseases & Institute of Bacterial Resistance & Institute of Infectious Diseases, Anhui Medical University, Hefei, Anhui, People's Republic of China

*These authors contributed equally to this work

Correspondence: Yanyan Liu; Gang Wang, Email liuyanyan725@ahmu.edu.cn; orthowanggang@163.com

Purpose: The formation of biofilms hinders direct contact between antibiotics and bacteria, reducing the efficacy of antibiotic therapy and presenting a substantial obstacle to the treatment of chronic osteomyelitis. To address this problem, we successfully constructed a chemically and structurally robust vancomycin-copper-tannic acid (Van@CuTA) antibiotic sustained-release system via a simple synthetic method, to target bacteria and inhibit biofilm formation.

Methods: Tannic acid (TA), copper ions (Cu^{2+}), and vancomycin hydrochloride (Van) were mixed and stirred at a low temperature to afford Van@CuTA nanospheres. Their antibacterial activity was evaluated against methicillin-resistant *S. aureus* (MRSA) using the Oxford cup method and live/dead bacterial staining. Their anti-biofilm activity was assessed via FE-SEM observations. Cell viability was assessed via MTT assay and osteogenic activity was detected via Western blotting (WB) and alkaline phosphatase (ALP) staining after co-culture with MG-63 cells. In vivo tibia-induced osteomyelitis model in rabbits was conducted to further validate the efficacy of Van@CuTA in treating osteomyelitis.

Results: The developed nanospheres exhibited drug release properties, with TA being released from the carrier and inhibiting the formation of bacterial biofilms. In vivo experiments demonstrated inhibition of MRSA biofilm formation through the encapsulation of TA within fibrin and its sustained release, followed by the sequential release of Van and Cu^{2}+ to directly eradicate MRSA. Moreover, Van@CuTA effectively promoted cell proliferation and bone formation. Van@CuTA is a multifunctional system that integrates biofilm targeting, drug release, antimicrobial activity, and cuproptosis-like bacterial death.

Conclusion: This study offers a novel and promising strategy for the development of antimicrobial agents to combat MRSA-induced chronic osteomyelitis.

Keywords: biofilm, osteomyelitis, copper ion, osteogenesis, antibacterial material

Introduction

Osteomyelitis is a bone infection characterized by inflammation, typically resulting from the spread of infection from surrounding tissues, trauma, surgical contamination, or systemic bacteremia.[1] Posttraumatic osteomyelitis (PTO) represents a significant subset of osteomyelitis cases. In China, traffic accidents account for up to 30 % of the primary injury factors associated with PTO.[2] Given the relatively thin coverage provided by the skin and subcutaneous tissue, the tibia and fibula of the lower extremities are particularly common sites of infection. Among the pathogenic microorganisms causing osteomyelitis, *Staphylococcus aureus* (*S. aureus*) is by far the most prevalent.[3] *S. aureus* secretes numerous extracellular and cell-associated virulence factors that facilitate adhesion, immune evasion, invasion, and penetration.[4] Importantly, *S. aureus* infects osteoclasts, macrophages, and other cells, proliferating within them to evade immune system clearance.[5,6] Additionally, it can form biofilms. Acting as a diffusion barrier, biofilms can impede the penetration

Received: 8 July 2025
Accepted: 2 November 2025
Published: 11 November 2025

of antimicrobial drugs and nutrients, thereby contributing to antibiotic resistance.[7] Furthermore, they hinder direct antibiotic contact with bacteria at the infection site, thus reducing their efficacy. Up to 47 % of cases of *S. aureus* osteomyelitis are caused by MRSA strains.[2]

Vancomycin is a glycopeptide antibiotic that exerts its effects by inhibiting the cross-linking of peptidoglycan precursors and mature polysaccharide layers.[8] This inhibition ultimately disrupts the synthesis of peptidoglycan in bacterial cell walls. The resulting disruption leads to defects in the cell wall, which subsequently culminates in bacterial death. As one of the antibiotics approved by the FDA for the treatment of MRSA infections, vancomycin presents several advantages: it is readily accessible, well-known among clinicians, and cost-effective.[9] However, meticulous drug monitoring is essential to mitigate the risk of nephrotoxicity. Even Van, which is clinically used to treat MRSA-induced osteomyelitis, may lead to the emergence of Van-resistant *S. aureus* (VRSA). Standard treatment for chronic osteomyelitis includes thorough early-stage debridement, removal of necrotic tissue, and administration of appropriate antimicrobial agents, either systemically or locally.[10,11] However, the attainment of optimal bactericidal effects with antibiotics continues to pose significant challenges due to the formation of biofilms.[12] To combat antibiotic-resistant bacteria, developing novel antibiotics or enhancing the susceptibility to existing.[13,14] Given the slow pace of new drug development and the rapid rise in antibiotic resistance, alternative therapies are crucial for osteomyelitis management.[15–17] Antibacterial materials capable of preventing or disrupting biofilm formation represent a promising research field for preventing early stage osteomyelitis from progressing to chronic osteomyelitis.[18–20]

Tsvetkov et al clearly demonstrated that excessive copper (cuprotosis) can induce cell death by targeting lipoylated proteins of the tricarboxylic acid (TCA) cycle.[21] This mechanism has been extensively investigated, revealing that the targets of copper-induced cytotoxicity are evolutionarily conserved across species, from bacteria to humans. Such findings suggest that the antimicrobial activity of copper ions may be universally applicable.[22,23] Furthermore, Karygianni et al demonstrated that the dense architecture of biofilms hinders the penetration of antimicrobial drugs, while the acidic, hydrogen peroxide-containing microenvironment within biofilms suppresses the immune response.[24] These insights have driven the advancement of drug delivery systems tailored to target bacterial biofilms, catalyze the in situ generation of reactive oxygen species (ROS), compromise biofilm integrity, and integrate bacterial cell wall-degrading agents. Such approaches aim to address the diminished efficacy of single antimicrobial agents due to biofilm formation and significantly enhance the synergistic antibacterial effect.[25,26] For example, copper-doped polyoxometalate clusters have demonstrated potential in addressing biofilm-associated infections by inducing a copper-poisoning-like death mechanism in bacteria.[27]

TA, also referred to as tannin, belongs to a class of natural polyphenols rich in pyrogallol and catechol groups. It's structural properties confer strong antioxidant properties, excellent antibacterial activity, and the capacity to promote cell proliferation, tissue regeneration, and wound healing.[28,29] TA can significantly enhance the anti-staphylococcal efficacy of beta-lactam antibiotics by inhibiting *S. aureus* biofilms.[30] Nanoparticle systems incorporating TA have demonstrated effective in vivo and in vitro MRSA biofilm eradication while maintaining good biocompatibility.[31] TA is rich in hydroxyl and carboxyl groups, and can form chelates with various metal ions (Ag^{+}, Cu^{2+}, Mg^{2+}, Zn^{2+}, Fe^{3+}, Eu^{3+}, Au^{3+}),[32–38] enabling responsive drug release under different environmental conditions, while retaining both TA and metal ion biological activities.

In this study, a simple solution-based method was developed to construct a topical drug delivery system targeting planktonic bacteria and biofilms in infectious environments. The metal polyphenol network (MPN) serves as a shell for encapsulating non-resistant antimicrobial peptides, while TA binds to bacterial surfaces through its affinity for the cell wall. The synthesized antibacterial nanospheres were encapsulated in fibrin sealant. During this process, the robust structure of the MPNs enabled the slow dissolution of the material, releasing Cu^{2+} and Van, which led to bacterial death. Through slow drug release, Van@CuTA effectively eradicated bacteria and inhibited biofilm formation. In vivo experiments demonstrated its strong antibacterial activity and bone-repair capabilities. Overall, this study highlights the efficacy and durability of Van@CuTA in eliminating MRSA and suppressing biofilm formation, offering a novel strategy for treating biofilms and resistant planktonic bacteria that hinder osteomyelitis healing.

Materials and Methods

Reagents

Vancomycin hydrochloride was purchased from MCE (China). Copper chloride ($CuCl_2$), TA, ascorbic acid, and dexamethasone were obtained from Aladdin (China). Fibrin sealant (Human) was purchased from Shanghai RAAS (China). The titanium sheets (purity > 99.5 %) were purchased from Qinghe County Jin'ou Metal Materials Co., Ltd. (China). 2.5 % glutaraldehyde fixed solution was purchased form Labcoms (USA). Mueller Hinton Broth (MHB) and Mueller Hinton Agar (MHA) were purchased from Thermo Scientific™ Oxoid™ (USA). Dimethyl sulfoxide (DMSO), thiazolyl blue tetrazolium bromide (MTT), and the live/dead bacteria staining kit (100 T) were obtained from Solarbio (China). β-Glycerophosphate disodium salt hydrate and pentobarbital sodium salt were purchased from Sigma-Aldrich (USA). Phosphate-buffered saline (PBS) was acquired from Biosharp (China).

Nanospheres Preparation

The Van@CuTA nanospheres were prepared via a simple solution method. First, 4 mg of $CuCl_2$ was dissolved in 40 mL of double-distilled water and stirred at room temperature (RT, about 25 °C) for 1 h. Then, 4 mg of TA and 4 mg of Van were added, and the mixture was stirred at 4 °C for 24 h. After centrifuging at 10,000 rpm for 10 min, an earthy yellow precipitate was obtained.[39] Discard the supernatant and resuspend in double-distilled water. The blank formulation (CuTA) was prepared using the same method, but without the Van. The CuTA and Van@CuTA obtained from the coprecipitated/coordinated polymer were stored at 4 °C until further analysis.

Materials Characterization

The surface morphology of the prepared Van@CuTA was characterized using transmission electron microscopy (TEM, Thermo scientific Talos L120C G2, USA) and field-emission scanning electron microscopy (FE-SEM, ZEISS Gemini SEM 300, Germany).[40,41] After synthesis, both CuTA and Van@CuTA were allowed to stand at 4 °C and RT. At specific time intervals (0, 1, 3, 5 d), the variations in particle size and polydispersity index (PDI) were monitored to assess the post-synthesis stability of the materials. The average particle size and PDI were determined via dynamic light scattering (DLS) analysis using a Zetasizer Lab (Malvern, UK) (n = 3).[42] The samples were diluted 50 to 100 times with double distilled water before measurement.

In vitro Antibacterial Efficiency

In this study, MRSA (ATCC 43300) was used as the experimental strain. Single colonies were transferred to MHB after resuscitating cryopreserved strains from MHA. The Oxford cup method was used to determine the diameter of the inhibition zone (IZ).[43] The MHA was adjusted to pH 5, and the bacterial suspension was evenly spread. The MHA plates spread with bacterial suspensions were divided into four groups: PBS group, Van group, CuTA group, and Van@CuTA group. The experimental concentrations of Van group and Van@CuTA group included 1 mg/mL, 0.5 mg/mL and 0.25 mg/mL. Three Oxford cups were placed on the plate at a distance of 2 cm, followed by the addition of 200 μL of fibrin sealant with PBS, Van, CuTA, and Van@CuTA (n = 3). After 2 d, the IZ diameter was measure using a millimeter ruler to evaluate the in vitro antibacterial activity of Van@CuTA and the gelation ability of the fibrin sealant.

Live/Dead Bacterial Fluorescence Assay

To further validate the antibacterial properties of Van@CuTA against planktonic MRSA, a live/dead bacterial fluorescence assay was performed.[44] The turbidity of bacterial suspensions was measured and adjusted using the DensiCHEK plus turbidity meter (bioMérieux, France). Briefly, the instrument was calibrated and blanked with a sterile saline solution (0.85 % NaCl). Bacterial colonies were emulsified in saline to achieve an initial suspension. The suspension density was then measured with the DensiCHEK plus and adjusted to a value equivalent to 0.5 McFarland standard (approximately 1.5×10^8 CFU/mL) by adding more bacteria or saline as needed. An MRSA suspension (500 μL, 9×10^8 CFU/mL) was co-incubated with 500 μL PBS, Van (1 mg/mL), CuTA (1 mg/mL) and Van@CuTA (1 mg/mL) for 2 d (n = 3). The supernatant was removed after centrifugation at 5000 g for 15 min and the bacteria were resuspended by adding 1mL of

0.85 % NaCl solution. Repeat that twice. The density of the bacterial suspension was adjusted to 1×10^8 CFU/mL. The bacteria were then incubated with NucGreen and EthD-III in the dark for 15 min. The samples were placed on glass slides, covered, and imaged using laser scanning confocal microscopy (Zeiss LSM 880, Germany) to assess bacterial viability. Live bacteria exhibited green fluorescence, whereas dead bacteria showed red fluorescence.

Biofilm Formation Imaging

Biofilm formation on titanium sheets was evaluated using FE-SEM.[45] The titanium sheets were cut into strips measuring 12 × 2 × 0.3 mm, then sterilized via autoclaving and dried in an oven for subsequent use. Titanium sheets were incubated with the prepared MRSA suspension (4.5×10^8 CFU/mL) at 37 °C to form biofilms (n = 3). At specific time points (1, 2, 3, 4, and 5 d), the sheets were collected for biofilm evaluation. Subsequently, the biofilms were fixed with a 2.5 % glutaraldehyde fixed solution at 4 °C for 12 h, followed by washing with PBS to remove any residual fixative. The biofilms were dehydrated using different ethanol gradients (30, 50, 70, 80, 90, and 100 %) at RT. After critical point drying (QUORUM K850, UK), the samples were sprayed with gold (Cressington 108Auto, UK) and examined via FE-SEM.

In vitro Antibiofilm Assay

The antibiofilm effect of Van@CuTA was further verified using FE-SEM. The biofilms cultured on the surface of the titanium sheets were exposed to 4 groups: PBS, Van (1 mg/mL), CuTA (1 mg/mL) and Van@CuTA (1 mg/mL) for 48 h (n = 3), and the same steps followed as described above.

Cell Culture

MG-63 cells (Procell Technology, China) were cultured in minimum essential medium (MEM) containing non-essential amino acids (NEAA) (Procell, China), supplemented with 10 % fetal bovine serum (Procell, China) and 1 % penicillin–streptomycin solution (Procell, China), in a humidified atmosphere of 5 % CO_2 at 37 °C.[46–48] For osteogenic differentiation, MG-63 cells were cultured in osteogenic differentiation medium (MEM including NEAA) supplemented with 10 % fetal bovine serum, 1 % penicillin–streptomycin solution, 200 μM ascorbic acid, 10 mM β-glycerophosphate disodium salt hydrate, and 100 nM dexamethasone.[15] The culture medium was refreshed twice per week.

Cell Viability Assay

The MTT assay was employed to assess cell viability. In brief, MG-63 cells were seeded into a 48-well plate 2×10^4 cells/well and incubated until adherence (n = 3). The original culture medium was subsequently substituted with an osteogenic differentiation medium supplemented with varying concentrations of Van@CuTA (0, 50, 100, 200, 400 μg/mL). Wells without nanospheres served as the control groups. After incubation for 1, 3, and 5 d, the cell density of each well was observed under an inverted microscope (CKX, Olympus). A 0.5 % MTT solution was then added, followed by incubation at 37 °C for 2 h. After removing the culture medium, DMSO (200 μL) was added and the plate was shaken for 10 min. The absorbance value was determined at a wavelength of 492 nm with the utilization of a microplate reader (BioTek ELx800 TM, USA).

Western Blotting

For total protein extraction, MG-63 cells were lysed in RIPA buffer (Beyotime, China), and the resulting lysate was centrifuged at 15000 × g for 10 min to remove cellular debris. Protein concentration was determined using the BCA Protein Assay Kit (Beyotime, China). Protein samples were subjected to SDS-PAGE, first at a constant voltage of 55 V for 1 h (based on Marker, Thermo Scientific™ PageRuler™, USA), then at 110 V until the target bands reached the middle of the gel. The membrane transfer apparatus was filled with the electrophoresis buffer and operated at a constant current of 200 mA; the transfer duration was adjusted according to the molecular weight of the target protein. Subsequently, the PVDF membrane was sequentially incubated with primary and secondary antibodies specific to the target proteins. After incubation with the ECL chemiluminescent solution (Beyotime, China), protein expression was visualized with a chemiluminescence imager, using GAPDH as the internal reference.

ALP Staining and Assay

ALP activity, a hallmark of early osteogenic differentiation, was visualized using a BCIP/NBT colorimetric kit (Beyotime, China). After co-culture with 200 μg/mL Van@CuTA for 7 and 14 days, MG-63 cells were rinsed with PBS and incubated with the ALP substrate solution (n = 3). Then the cell layers were then rinsed with ultrapure water, and microscopic images were acquired using an inverted microscope (Olympus CKX53, Japan).

Osteoblastic cells synthesize ALP, an enzyme that cleaves phosphate groups from *p*-nitrophenyl phosphate to produce *p*-nitrophenol (PNP). The absorbance of PNP serves as a biochemical indicator for evaluating the osteoblastic activity of cells cocultured with the nanospheres. Accordingly, ALP activity was further quantified using the ALP Assay Kit (Beyotime, China), and the absorbance of the resulting solution was measured at 405 nm with a microplate reader.

In vivo Experiments

All experimental protocols in this study were approved by the Ethics Committee of Anhui Medical University (LLSC20231459). Animal housing and procedures were performed in accordance with the "Guiding Principles for the Care and Use of Animals" (China).

In the in vivo experiment, 16 pathogen-free male New Zealand white rabbits at 4 months of age (mean weight = 2.76 ± 0.11 kg) were investigated, with a healthy control group included. The rabbits were randomly assigned to four groups: Normal group, PBS group, Fibrin Sealant group, and Van@CuTA group (n = 4). Following anesthesia with pentobarbital sodium (30 mg/mL), the bilateral hind limbs were shaved, disinfected with povidone-iodine skin cleanser, and covered with sterile drapes. A longitudinal incision measuring 1 cm was performed using a No. 10 blade at the proximal tibial metaphysis. Subsequently, a cortical bone window was created utilizing a 4-mm Kirschner wire. After removing the contents of the bilateral tibia cavities, 1 mL of 5 % sodium morrhuate (Hainan Unipul Pharmaceutical Co., Ltd., China) was injected. Titanium sheets that were submerged in an MRSA suspension for 48 h were employed to induce the osteomyelitis model.[49] The titanium sheets utilized in the Normal group were sterile. Following the placement of contaminated titanium sheets, 200 μL of 1 X PBS was injected into the medullary cavity for the PBS group. In the Fibrin Sealant group and the Van@CuTA group, 200 μL of fibrin sealant was administered without or with final concentration of 200 μg/mL Van@CuTA, respectively. The medullary cavity was then occluded using bone wax, after which the incision was sutured, disinfected, and dressed.[50]

At 28 d post-surgery, the rabbits were euthanized via intravenous administration of 2.5 mL pentobarbital sodium (200 mg/mL), and their tibias were harvested for subsequent analysis.[51] All animals were housed in a standard laboratory environment with ventilated room, a temperature of 25 ± 1 °C, humidity of 60 ± 5 %, and a 12 h light-dark cycle, with unrestricted access to water and food.

FE-SEM Characterization and Microbiological Evaluation

On 28 d, the following are the brief procedures for aseptically collecting secretions from the incision site: Disinfect the skin surrounding the incision with 75 % ethanol. Gently insert a sterile cotton swab into the basal part of the incision and rotate it to absorb the purulent fluid. Promptly transfer the collected sample into a sterile EP tube containing 1 mL of PBS. Vortex the sample vigorously for 2 min to homogenize the bacterial suspension. Dip a sterile spreader into the suspension and spread it onto MHA plate (n = 3). Then, incubate the plate at 37 °C for 24 hours.

After the incision secretion has been collected, the implanted titanium sheets were carefully retrieved (n = 3). Subsequently, the biofilms were fixed with a 2.5 % glutaraldehyde fixed solution at 4 °C for 12 h, followed by washing with PBS to remove any residual fixative. The biofilms were dehydrated using different ethanol gradients (30, 50, 70, 80, 90, and 100 %) at RT. After critical point drying (QUORUM K850, UK), the samples were sprayed with gold (Cressington 108Auto, UK) and examined via FE-SEM. Mass spectrometry (VITEK® MS, French) was used to verify the bacterial species.

Radiographic Analysis

To evaluate bone infection, digital X-ray and computed tomography (CT) images of the tibias were obtained (n = 3). CT scans were acquired in the sagittal, coronal, and axial planes. The RadiAnt DICOM Viewer was then used for 3D

reconstruction. Changes in the intramedullary and soft-tissue signals, the presence of subperiosteal and/or extraperiosteal fluid collections, and the formation of soft-tissue abscesses were assessed. The Odekerken scoring system was employed to evaluate osteomyelitis-related manifestations.[52]

General Observations

Postoperatively, the body weight was monitored every 2 d. The surface morphology of the harvested tibial specimens was examined macroscopically, and local features at the incision site were documented concurrently (n = 3).

Histological Evaluation

For histological staining, the harvested tibial specimens were first fixed with 4 % paraformaldehyde, then decalcified with ethylenediaminetetraacetic acid (EDTA), followed by dehydration through a graded ethanol series, and finally embedded in paraffin (n = 3). Longitudinal sections (approximately 5 μm thick) were taken from the upper middle portion of each tibia and examined under a transmission light microscope.

Statistical Analysis

The mean ± standard deviation (SD) was used to present quantified data and each experiment was performed in triplicate or more ($n \geq 3$). Statistical analysis of data was completed with *GraphPad Prism* software. The statistical significance of the differences was obtained through the parametric test (*Student's t*-test or *ANOVA*) and non-parametric test (*Mann–Whitney U*-test or *Kruskal–Wallis T* test). $p \leq 0.05$ considered statistically significant, indicated as* for $p < 0.05$, ** for $p < 0.01$, and *** for $p < 0.001$.

Results

Synthesis and Characterization of Van@CuTA

The Van@CuTA nanospheres were synthesized via a simple solution method, as shown in Figure 1A. Cu^{2+} formed coordination bonds with TA, enabling cross-linking end encapsulation of Van via co-precipitation.[33]

As shown in Figure 1B, the synthesized Van@CuTA can be readily dispersed in an aqueous solution, giving rise to a stable and homogeneous earth brown colloidal suspension. A notable concentration-dependent color intensification phenomenon can be witnessed. The color gradually evolves from a light tan at 50 μg/mL to a deep tan at 2 mg/mL. This visual gradient not only validates the successful synthesis of the nanospheres but also attests to its excellent dispersibility and the increasing density of nanospheres within the solution.

Both FE-SEM and TEM were employed, revealing the amorphous structure of Van@CuTA. TEM and FE-SEM images of Van@CuTA revealed a spherical diameter similar to that of the hydrodynamic size measured using DLS (Figure 1C). Notably, a loose net-like shell covering the nanocore was observed in the TEM image, confirming the formation of the CuTA complex around Van nanocrystals. Moreover, the FE-SEM image of Van@CuTA indicated that the MPN was a homogenous and cross-linked system.

As depicted in Figure S1, all synthesized specimens were furnished the DLS intensity distribution plots, namely CuTA and CuTA@Van. All the samples display a single, relatively narrow peak. This indicates that nanospheres exhibit excellent dispersibility and homogeneity within the dispersion medium, ruling out the presence of a mixture of multiple particle size populations. The Z-average particle size of CuTA measures 227.0 ± 6.2 nm, with a PDI of 0.429 ± 0.044, thereby demonstrating remarkable monodispersity. Subsequent to the encapsulation of Van, the particle size of Van@CuTA increases to 430.8 ± 9.7 nm, with a PDI of 0.520 ± 0.055. This increase in particle size serves as compelling evidence for the successful encapsulation of Van by CuTA.

As in Figure 1D, both CuTA and Van@CuTA exhibited acceptable stability during storage at 4 °C for 5 d, with no visible crystallization or agglomeration. Furthermore, the particle size and PDI did not change significantly. Even after 3 d at RT, both formulations maintained acceptable diameters, indicating that Van@CuTA possesses good physical stability for storage and transportation at low temperatures. Compared to conventional stabilizers, CuTA conferred superior physical stability to Van.

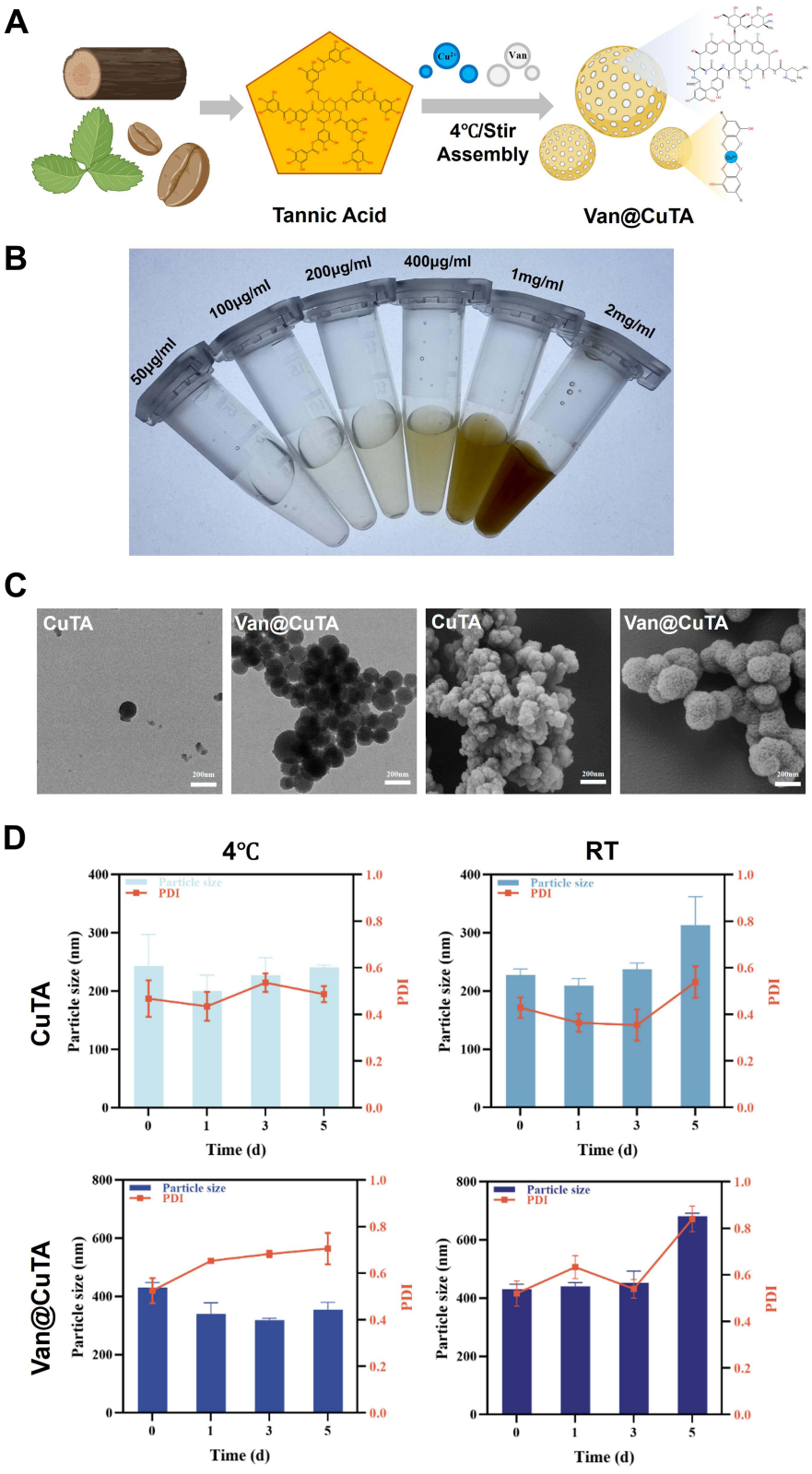

Figure 1 Synthesis and characterization of the Van@CuTA nanospheres. (**A**) Schematic diagram illustrating the synthesis principle. (**B**) Digital photograph of the earthy brown Van@CuTA nanospheres dispersed in double-distilled water at varying concentrations (from left to right: 50, 100, 200, 400, 1000, and 2000 μg/mL). The volume in each EP tube is 500 μL. (**C**) TEM and FE-SEM images of CuTA and Van@CuTA. (**D**) Stability of CuTA and Van@CuTA evaluated at 4 °C and RT over 5 d, characterized by particle size and PDI. All data were presented as means ± SD (n = 3).

https://doi.org/10.2147/IJN.S548765

Van@CuTA Interaction with Bacteria in vitro

As shown in Figure 2A and Table 1, compared with CuTA, Van@CuTA exhibited relative antibacterial activity against MRSA. The IZ values of Van at gradient concentrations were 1.8, 1.6 and 1.2 cm, while those for Van@CuTA at the same concentrations were 1.4, 1.2 and 1.0 cm. These results clearly suggest the antibacterial effect of Van@CuTA against MRSA.

Live/dead bacterial staining further demonstrated the antimicrobial properties of CuTA and Van@CuTA (Figure 2B). Fluorescence staining of live and dead tissues was performed using NucGreen (green fluorescence) and EthD-III (red fluorescence). Statistical analysis of the red/green fluorescence intensity indicated that Van@CuTA at a concentration of 1 mg/mL exhibits superior bactericidal efficacy against MRSA compared to the use of either Van or CuTA alone at the same concentration (Figure 2C), highlighting the significant antibacterial properties of Van@CuTA.

FE-SEM analysis was performed to investigate the spatial organization of biofilms and the distribution of extracellular polymeric substances (EPS) (Figure 2D). After 24 h of incubation, only sparse bacterial adhesion was observed on the titanium sheets, corresponding to the initial adhesion stage. After 24–48 h of incubation, the cells produced more EPS and formed immature honeycomb-like structures. After prolonged incubation for 48–72 h, mature 3D biofilm architectures were observed, consisting of dense microcolonies embedded in a complex EPS matrix (maturation stage). After 72–96 h of incubation, biofilm dispersion began, with individual bacteria detaching into the surrounding environment due to the EPS degradation. Both intact and damaged bacteria were observed on the titanium sheets at this dispersion stage. Briefly, the MRSA strain followed a typical biofilm life cycle: attachment, microcolony formation, development, maturation, and dispersion.

To investigate the antibiofilm mechanism of Van@CuTA, changes in MRSA morphology after treatment with PBS, Van, CuTA, and Van@CuTA were examined using FE-SEM (Figure 2E). Untreated MRSA biofilms exhibited typical honeycomb-like structures. After Van treatment, residual rough biofilm-like structures were still visible, with a small number of bacteria remaining on the Van-treated titanium surface. CuTA-treated surfaces showed clump-like deposits, possibly representing CuTA bound to the biofilm. However, after treatment with Van@CuTA, almost no honeycomb-like structures were present on the surface of the titanium sheet. The bacterial surface collapsed and became wrinkled, indicating that the biofilm was barely formed, and the bacterial membrane was severely damaged.

Van@CuTA Interaction with Osteoblast Cells in vitro

Minimal cytotoxicity is essential for materials used in tissue engineering applications. To estimate the potential cytotoxic effects of Van@CuTA, the viability of MG-63 cells was investigated using the MTT assay at varying concentrations (50, 100, 200, 400 μg/mL) of extract from the composites (Figure 3A). After 5 d of incubation, no significant cytotoxicity was observed at concentrations up to 400 μg/mL. In fact, cell viability increased with increased Van@CuTA concentrations, indicating favorable cytocompatibility. However, at 400 μg/mL, a slight decrease in cell viability was noted, although no signs of cytotoxicity were observed.

The effect of the Van@CuTA nanospheres on osteogenesis-related proteins was investigated by analyzing the expression of RUNX2 at the protein level (Figure 3B) after 7 and 14 d of co-incubation with MG-63 cells.[53] WB analysis showed that RUNX2 expression was significantly higher in the Van@CuTA group compared to the control group (Figure 3C). Therefore, the developed nanospheres exhibited superior biocompatibility and excellent osteogenic effects.

Additionally, the ability of the Van@CuTA nanospheres to stimulate mineralization in MG-63 cells was analyzed via ALP staining after 7 and 14 d of induction (Figure 3D).[54] The Van@CuTA group exhibited a greater number of blue-stained nodules with more intense coloration, with quantitative analysis (Figure 3E) revealed that Van@CuTA significantly enhanced ALP expression.

Van@CuTA Eliminates Bacterial Infections in vivo

Considering the ability of Van@CuTA to target the surface of Gram-positive bacteria, the co-release of TA and Van can disrupt the bacterial biofilm, while bacterial internalization of Cu^{2+} induces cuproptosis-like bacterial death. Therefore, bone marrow infections caused by MRSA can be effectively treated using this solution.

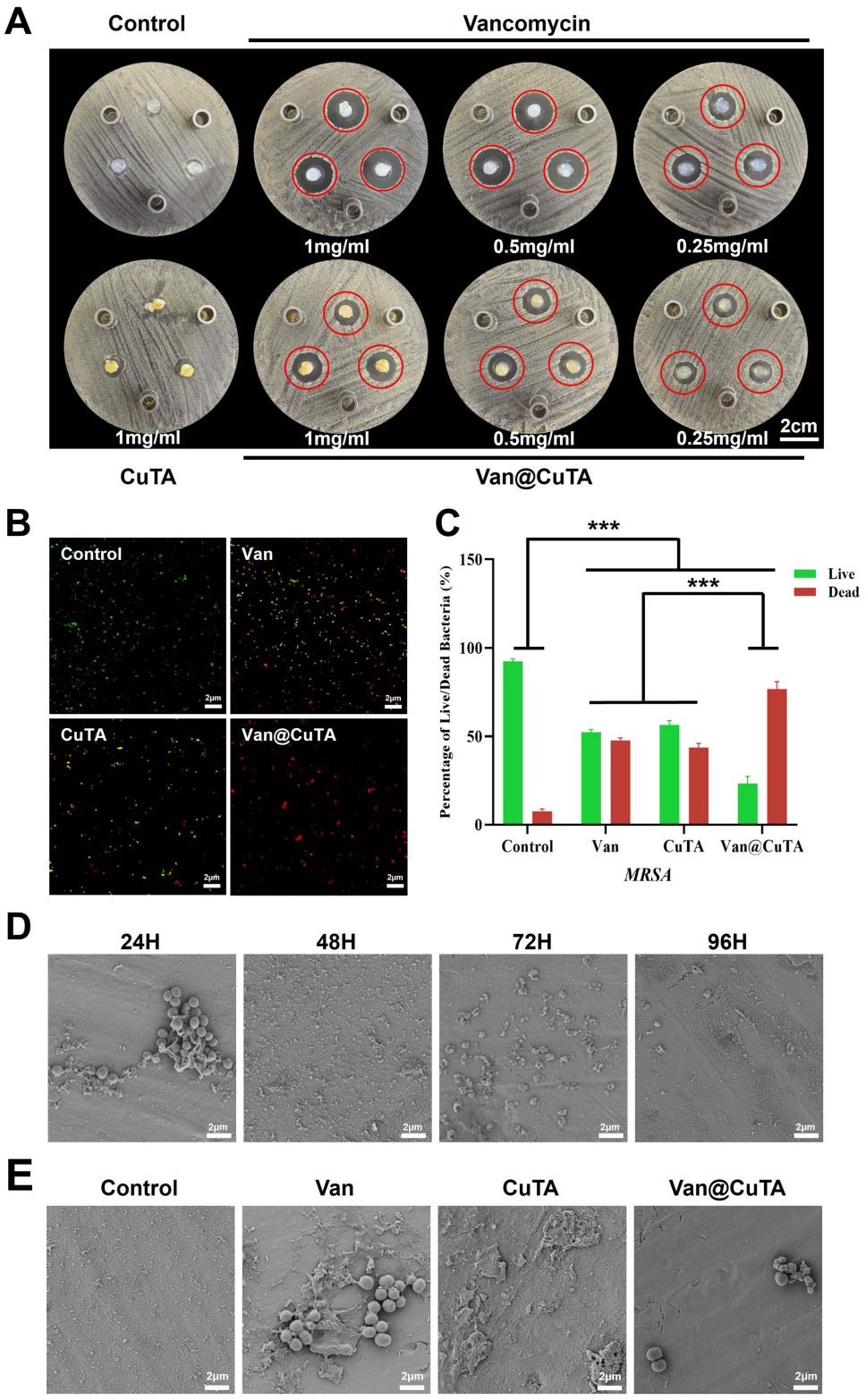

Figure 2 In vitro antibacterial properties of Van@CuTA. (**A**) Digital images of MRSA Oxford cup assays after different treatments. Red circles of the same size mark the boundaries of the inhibition zones (scale bar, 2 cm). (**B**) Fluorescence images showing surviving (green) and dead (red) bacteria (scale bar, 2 μm). (**C**) Quantification of live (green) and dead (red) fluorescence intensities. (**D**) FE-SEM images of MRSA biofilms at different stages. (**E**) FE-SEM images of MRSA after 48 h of different treatments. All data were analyzed using one-way *ANOVA* and presented as means ± SD (n = 3, ***$p < 0.001$).

https://doi.org/10.2147/IJN.S548765

Table 1 Table of the Measurement Data for Inhibition Zones of Different Treatment Groups. All Data Were Presented as Means ± SD (n = 3)

Groups	Control	Van			CuTA	Van@CuTA		
		1mg/mL	0.5mg/mL	0.25mg/mL	1mg/mL	1mg/mL	0.5mg/mL	0.25mg/mL
Inhibition zone size(cm)	0	1.8±0.3	1.6±0.3	1.2±0.1	0	1.4±0.2	1.2±0.1	1.0±0.1

Compared with the normal group, the PBS-treated group exhibited skin swelling and ulceration near the incision site, while the fibrin gel group showed skin swelling (Figure 4A). Conversely, the Van@CuTA group exhibited no obvious signs of infection.

At 28 d, examination of the infected tibias revealed yellow abscesses and bone erosion in the PBS and Fibrin gel groups, respectively (Figure 4B). In contrast, the tibias in the Van@CuTA group appeared normal, indicating near-complete eradication of infection in this group.

By 28 d, the incisions had almost completely healed, and bacterial survival was further investigated by using the diffusion plate method. Compared with the PBS and Fibrin gel groups, the Van@CuTA group had a significantly lower number of colonies (Figure 4C).

To confirm the pathogen of the established infection model, we conducted mass spectrometry analysis on the bacterial isolates recovered from the exudates of the three groups of animals. As presented in Supplementary Figure S2, the mass spectra of all three isolates were unambiguously identified as Staphylococcus aureus, with a confidence level exceeding 99.9 %, thereby validating the specificity of our infection model.

FE-SEM was employed to investigate biofilm formation. As shown in Figure 4D, in the normal group, only red blood cells were observed on the surfaces of the titanium sheets. Compared to the PBS and Fibrin gel groups, the Van@CuTA-treated sheets barely formed biofilms, with minimal bacterial presence and red blood cells.

Van@CuTA Accelerated Bone Healing in vivo

During the treatment period, the body weight of the rabbits was monitored every two days (Figure 5A), with rabbits in the Van@CuTA group gaining weight as slowly as those in the Normal group. Conversely, rabbits in the remaining groups exhibited a marked reduction in body weight during the initial phase of treatment. Blood analysis at 28 d (Figure 5B) revealed that the white blood cell (WBC), monocyte (MON), and neutrophil (NEU) count in the Van@CuTA group were closest to Normal, suggesting significantly alleviated inflammatory response.

Radiographic assessments were conducted to evaluate manifestations of osteomyelitis infection.[55] After 28 d, the Normal group showed no signs of abnormal tibial morphology and exhibited the minimal extent of the bone defect (Figure 5C). In contrast, the Van@CuTA group displayed mild or no periosteal reaction and showed closure of the defect by day 28. Conversely, the PBS and Fibrin gel groups exhibited classic features of chronic osteomyelitis, including periosteal reaction, osteolysis near the metaphyseal region, and diaphyseal osteolysis accompanied by cortical resorption.

Histological evaluation using hematoxylin-eosin (HE) staining revealed visible retention of a large number of inflammatory cells—including lymphocytes, multinucleated giant cells, and neutrophils—in the bone marrow of the PBS and CuTA groups on 28 d (Figure 5D). By comparison, the infiltration of inflammatory cells in the Van@CuTA group was markedly reduced, suggesting that the synergistic antibacterial activity of Cu^{2+}, TA, and Van effectively eliminated MRSA-induced osteomyelitis.

Goldner's staining was employed to assess new bone formation and mineralization of the bone matrix in the tibias at 28 d. The Normal group exhibited a well-organized, newly formed bone matrix surrounding the tibia, with osteocytes enclosed within osteogenic lacunae. In contrast, the PBS and CuTA groups showed significantly fewer osteocytes embedded in the new bone matrix, along with disrupted matrix architecture. Notably, the Van@CuTA group exhibited a new bone matrix structure similar to that of the normal group.

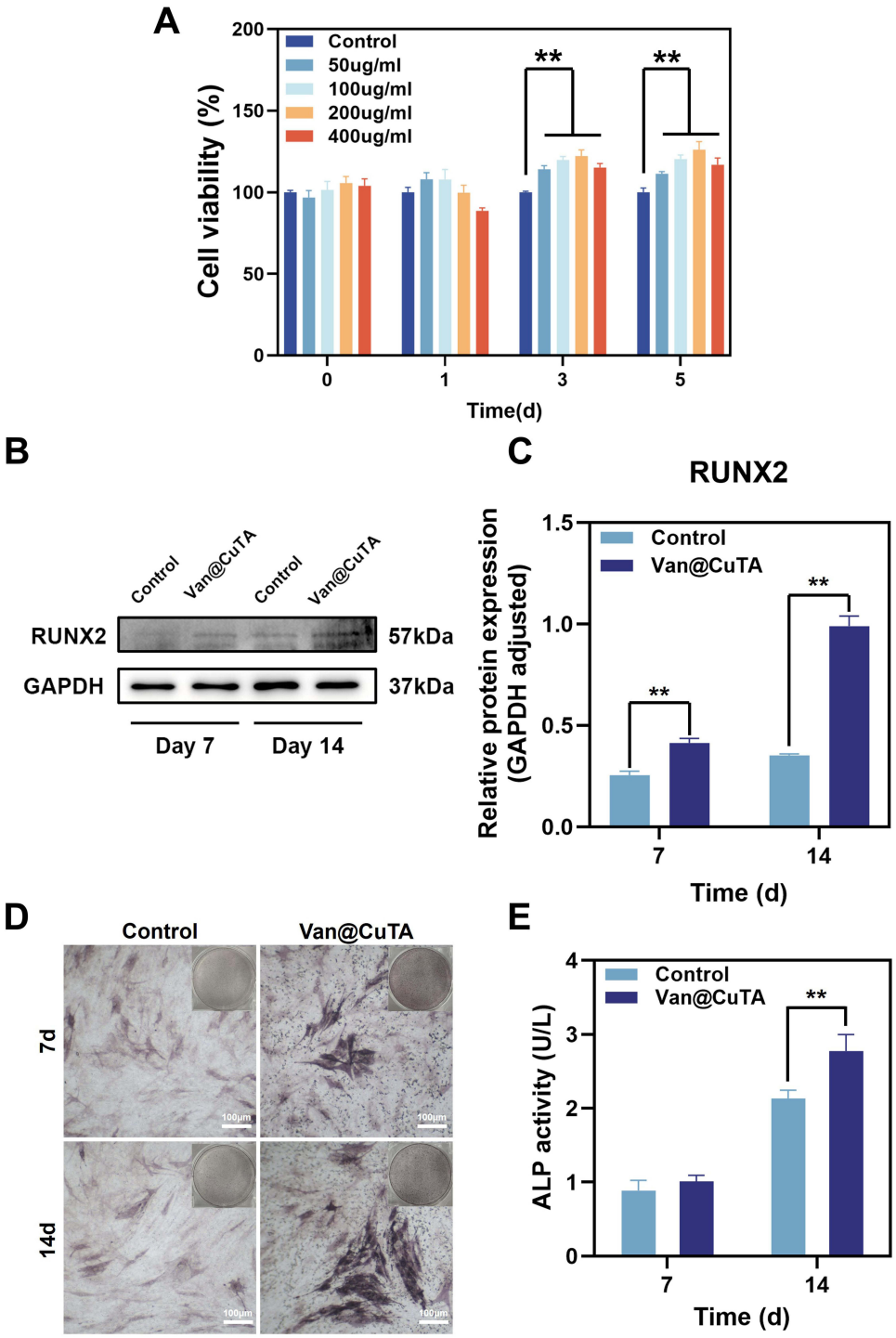

Figure 3 Biocompatibility and promotion of osteogenesis in MG-63 cells. (**A**) MTT assay results showing viability of MG-63 cells after various treatments. (**B**) Western blot analysis of RUNX2 expression in MG-63 cells post-treatment. (**C**) Quantitative analysis of relative RUNX2 expression in MG-63 cells after treatments. (**D** and **E**) Representative ALP staining images and quantitative evaluation of ALP activity in MG-63 cells (scale bar, 100 μm). All data were analyzed using one-way *ANOVA* and presented as means ± SD (n = 3, $^{**}p < 0.01$).

Discussion

In this study, we constructed a metal polyphenol-antibiotic co-delivery system with a dual-mode antibacterial mechanism via a simple solution-based method. TA specifically targets MRSA and its biofilms through chemical coordination, while the locally released Cu^{2+} and Van exert a dual bactericidal effect by inducing copper toxicity-like cell death and

https://doi.org/10.2147/IJN.S548765

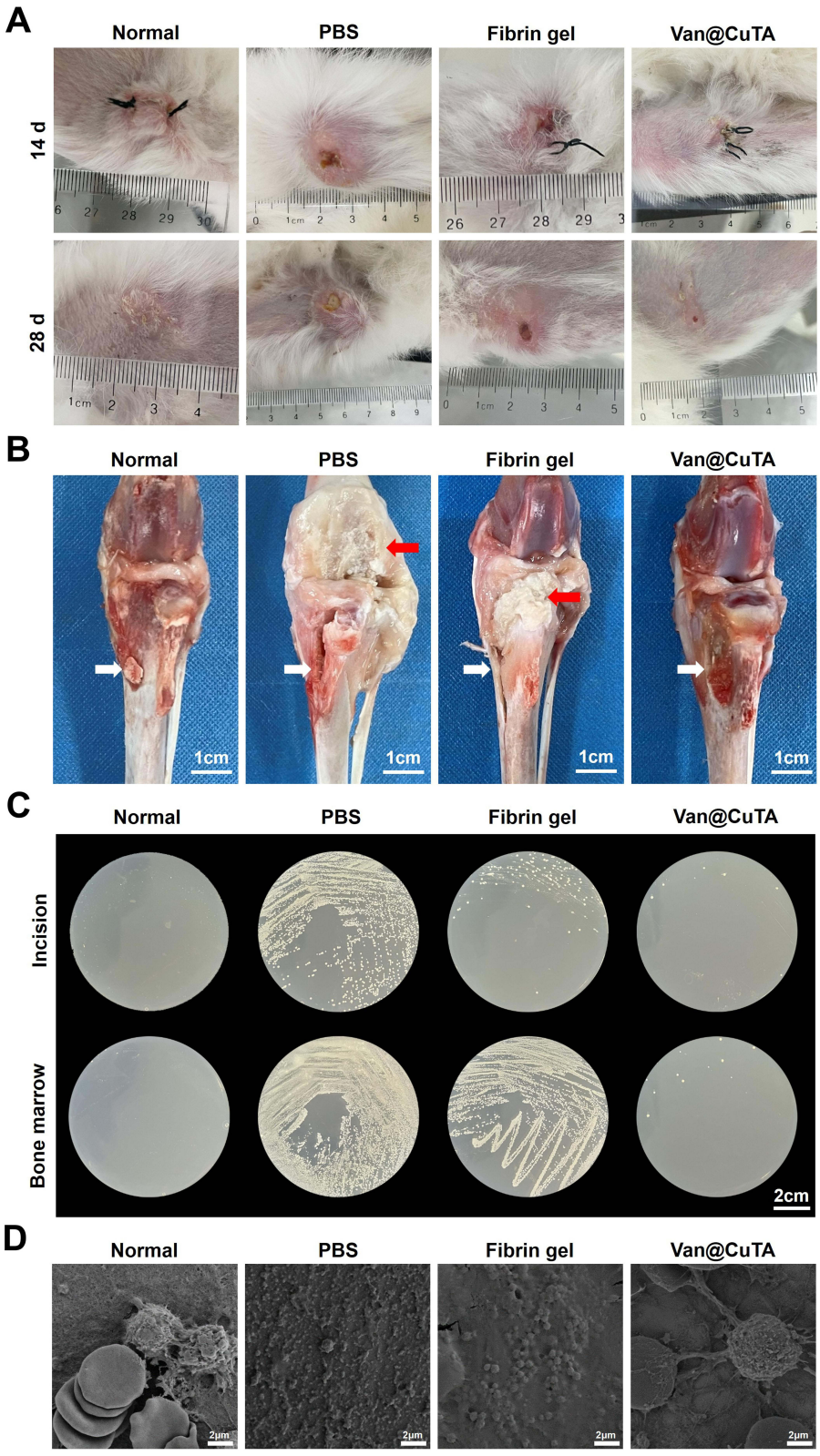

Figure 4 In vivo therapeutic effect of Van@CuTA on MRSA-infected osteomyelitis. (**A**) Photographs of surgical incisions at 14 and 28 d post-operation. (**B**) Representative images of rabbit tibias after various treatments. White arrows point to the bone defect while red arrows point to the regions of bone destruction. (**C**) Representative plate images showing MRSA isolated from incision sites and bone marrow. (**D**) Representative FE-SEM images of titanium sheet surfaces (scale bar, 2 μm).

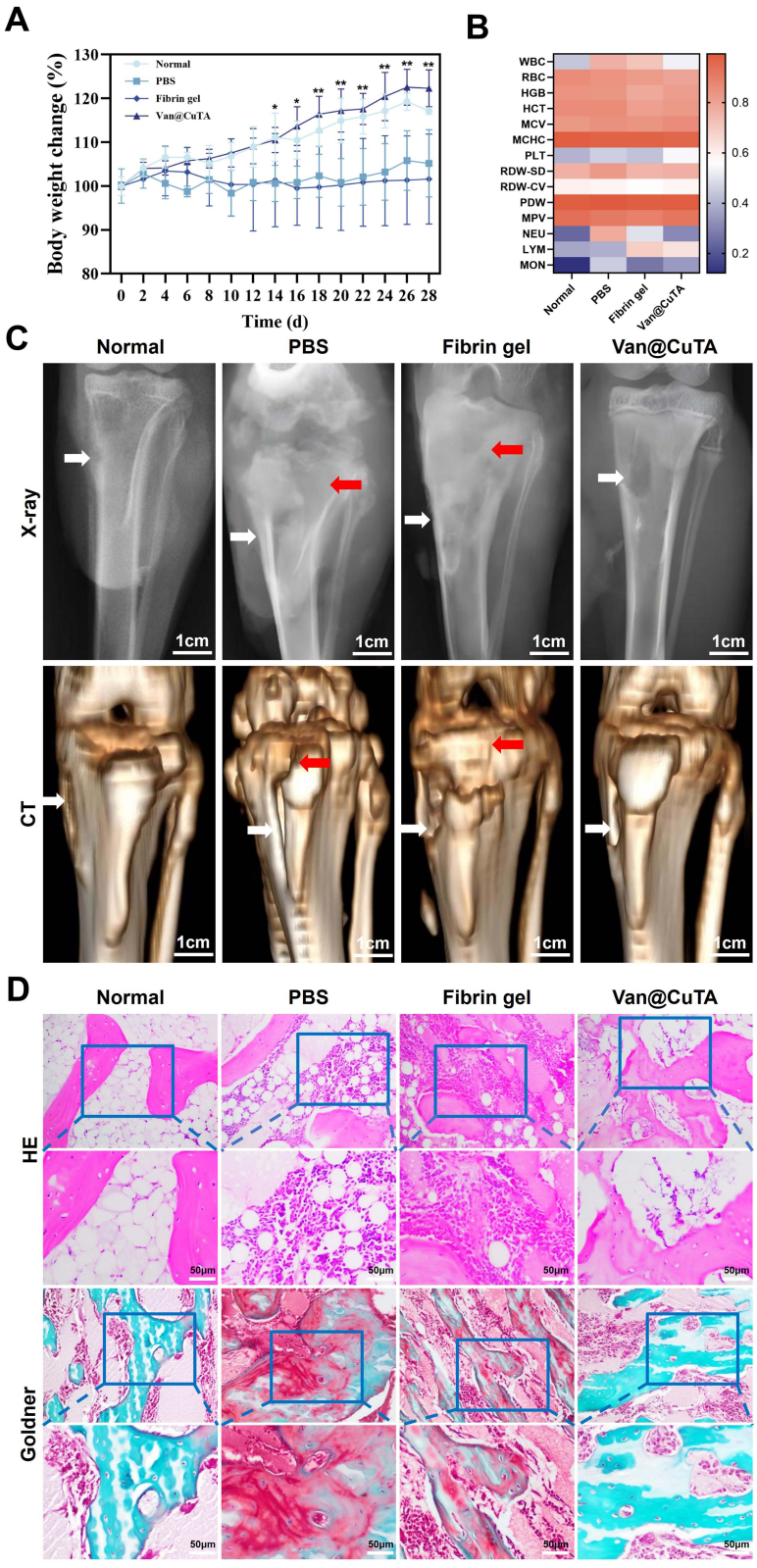

Figure 5 Osteogenesis-promoting ability of Van@CuTA in vivo. (**A**) Changes in body weight following different treatments. (**B**) Blood routine test results on day 28 after treatments. (**C**) Representative X-ray and CT images of post-treatment rabbits. White arrows point to the bone defect while red arrows point to the regions of bone destruction. (**D**) HE and Goldner staining of tibia samples following treatments. All data were analyzed using one-way *ANOVA* and presented as means ± SD (n = 3, *$p < 0.05$, **$p < 0.01$, Van@CuTA group compared to PBS group and Fibrin Sealant group).

https://doi.org/10.2147/IJN.S548765

inhibiting cell wall synthesis, respectively. In order to accomplish local high-concentration drug delivery and spatial anchoring at the infection site, thereby surmounting the issues of nanosphere diffusion and loss, we encapsulated the synthesized antibacterial nanospheres within the fibrin sealant. Notably, the incorporation of non-antibiotic components effectively mitigated antibiotic resistance associated with biofilm formation. Furthermore, Van@CuTA not only promoted cell proliferation and accelerated bone healing, but also maintained excellent biocompatibility, offering a novel therapeutic strategy with anti-biofilm, bactericidal, and bone regeneration capabilities for the clinical management of chronic osteomyelitis.

TA, a natural polyphenol with abundant sources, has been extensively investigated for its antibacterial mechanisms, including inhibition of peptidoglycan, teichoic acid, and lipids synthesis, disruption of cell membranes, inhibit ribosome formation and interfere with the biosynthetic pathways of proteins and amino acids.[56] Owing to its pyrogallol/catechol groups and dendritic structure, TA can effectively chelate with various metal ions to form stable complexes under neutral or basic pH conditions. Zhang et al developed a grid-like structure by assembling TA and Cu^2+, which encapsulated disulfiram.[57] This innovative approach facilitated responsive release within the tumor microenvironment, thereby eliciting an anti-tumor effect. The CuTA nanosheets synthesized by Ha et al exhibit a stimulus-responsive release of the encapsulated drugs and Cu^2+ within an acidic environment characterized by a high concentration of glutathione.[58] This mechanism bears a resemblance to our design for antibiotic release under infection conditions. Hu et al employed gallic acid (GA), a hydrolysis product of tannic acid, to bind with Cu^2+ for coating Van intended for application in infected wounds.[26] As CuGA underwent degradation, Van was released, exerting functions such as sterilization, anti-inflammation, promotion of epidermal cell proliferation at the wound site, and angiogenesis.

The developed Van@CuTA system employs a TA-Cu^2+ coordination network as the coating carrier for loading sensitive antibiotics. The surface morphology and structure were analyzed via TEM and FE-SEM. Nanospheres with an amorphous structure and a rough surface were observed. Particle size and PDI measurements revealed that the stability of Van@CuTA decreased with increasing temperature, suggesting that the rapid local release of the encapsulated drug during in vivo application could expedite the achievement of minimum bactericidal concentration (MBC).

In vitro bacterial experiments demonstrated that the Van@CuTA system exerted a synergistic bactericidal effect by targeting both planktonic bacteria and biofilms within an infectious microenvironment. Live/dead fluorescence staining and FE-SEM imaging revealed that Van@CuTA exhibited superior antibacterial efficacy against MRSA and biofilm inhibition compared with free antibiotics. Mechanistic studies revealed that the TA phenolic hydroxyl groups can coordinate with teichoic acid in the cell walls of Gram-positive bacteria, enhancing bacterial adhesion. The chemical stability and pH responsiveness of the metal-polyphenol network enable controlled dissociation in acidic microenvironments, thus triggering the synergistic and sustained release of Cu^2+ and Van. During the targeting phase, Cu^2+ generates ROS through a Fenton-like reaction that compromises the integrity of the bacterial cell membrane, while Van specifically inhibits peptidoglycan synthesis in the cell wall, leading to an intracellular osmotic imbalance.[59] Moreover, the sustained release of Cu^2+ effectively degrades the extracellular polysaccharide matrix, enhancing the osmotic killing effect of Van on dormant bacteria within recalcitrant biofilms.[60]

In vitro cell experiments confirmed that the system not only promoted osteoblast proliferation, but also upregulated RUNX2 expression, thereby enhancing osteogenesis. This improved osteogenic differentiation may be attributed to either a reduction in local ROS levels or activation of the calcium signaling pathways. ROS is a known regulator of bone tissue regeneration and can impair osteogenic induction by downregulating key osteogenesis-related genes such as RUNX2, ALP, and BMP-2.[61] Furthermore, MPNs have been shown to effectively enhance the osteogenic differentiation of hASCs even under H_2O_2 exposure.[62] In vivo animal models demonstrated that Van@CuTA could significantly reduce bacterial load, alleviate inflammatory responses at the infection site, and promote bone defect repair.

Chronic osteomyelitis presents a formidable clinical challenge due to bacterial films that adhere to bone, shield pathogens from the effects of antibiotics and immune defense, thus promoting bone destruction.[63] Additionally, due to the low permeability and reduced blood flow of bone tissue, intracellular bacterial infection, and proliferation, effective treatment of chronic osteomyelitis requires antibiotics to penetrate hard bone structures, biofilms, and even host cells while maintaining adequate therapeutic concentrations locally.[64,65] The Van@CuTA system investigated in this study effectively inhibited bacterial growth and biofilm formation, significantly reduced bacterial counts in vivo and levels of

inflammatory cells in the blood, eradicated local inflammation, promoted osteoblast proliferation, and facilitated the repair of damaged bones. In vivo results revealed no evident bone destruction or sequestrum formation post-treatment, and marked new bone formation was observed, further validating its efficacy for bone repair.

In this study, we successfully demonstrated the excellent therapeutic effect of the constructed Van@CuTA in a rabbit model of chronic osteomyelitis. However, several significant technical limitations have somewhat impacted the comprehensive evaluation of Van@CuTA properties. Firstly, due to constraints associated with current detection methods, we were unable to accurately quantify the drug loading efficiency (DLE) and drug loading capacity (DLC) of Van. This limitation hindered our ability to thoroughly elucidate the quantitative relationship between drug loading and release behavior from a pharmacokinetic perspective. Secondly, while the pH-responsive release characteristics of the material design were preliminarily validated through in vitro antibacterial experiments, the absence of quantitative release kinetics data within complex physiological environments in vivo has restricted our understanding of Van@CuTA's intelligent drug release behavior. Finally, although MG-63 cells serve as a valuable osteogenic model for bone-related research, they do not fully replicate the behavior exhibited by human primary osteoblasts or osteoblasts derived from human pluripotent stem cells.

Despite these limitations, the therapeutic effect demonstrated by the Van@CuTA in the animal model was not significantly compromised, indicating that the functional design is effective at a broader level. However, to further enhance the clinical translation and application of Van@CuTA, future research must address several key aspects: on one hand, it is essential to develop a high-performance liquid chromatography-tandem mass spectrometry method for quantitatively measuring DLE and DLC. This will facilitate a multi-dimensional quantitative evaluation of drug loading performance and release kinetics; on the other hand, constructing a more comprehensive in vitro biomimetic environment model is crucial to simulate pH gradient changes within the infection microenvironment. Additionally, integrating this with in vivo real-time monitoring technology will allow for an in-depth exploration of the responsive drug release mechanisms of Van@CuTA under pathological conditions, thereby improving its controllability and reliability. Furthermore, future investigations should also encompass quantitative bacterial culture analysis as well as assessments of common clinical parameters through immunohistochemical and fluorescence staining techniques. We anticipate that these findings will yield comprehensive insights into the biological properties of Van@CuTA. Additionally, we explored CuTA's role as a Van carrier. Given the diverse array of pathogens associated with chronic osteomyelitis, it is imperative to further investigate other bacterial types and their potential interactions with various sensitive antibiotics. This approach will provide a more robust experimental foundation for subsequent clinical applications.

Conclusion

In summary, CuTA serves as an effective antibiotic carrier and is anticipated to facilitate the loading of other poorly water-soluble antibiotics, thereby enhancing the therapeutic efficacy against chronic osteomyelitis resulting from non-MRSA infections. The subsequent phase of this study will involve further validation of the safety and antibacterial properties of the nanospheres in large animal models, such as beagle dogs, providing essential data support for future clinical research.

Its potential clinical application as an alternative treatment for chronic osteomyelitis-related infections includes continuous in vivo and in vitro release of antibiotics, inhibition of bacterial growth and biofilm formation, as well as promotion of osteogenesis. This approach is expected to transform the traditional treatment paradigm for chronic osteomyelitis by preventing infection recurrence or secondary removal associated with conventional antibiotic bone cement. Ultimately, it aims to achieve complete resolution without necessitating lesion clearance while improving patient compliance and quality of life.

Abbreviations

TA, tannic acid; Cu^{2+}, copper ions; Van, vancomycin hydrochloride; MRSA, methicillin-resistant *S. aureus*; WB, Western blotting; ALP, alkaline phosphatase; PTO, posttraumatic osteomyelitis; *S. aureus, Staphylococcus aureus*; VRSA, vancomycin-resistant *S. aureus*; TCA, tricarboxylic acid; MHB, mueller hinton broth; MHA, mueller hinton agar; DMSO, dimethyl sulfoxide; FE-SEM, field emission scanning electron microscopy; TEM, transmission electron

microscopy; PDI, polydispersity index; DLS, dynamic light scattering; RT, room temperature; IZ, inhibition zone; PBS, phosphate buffered saline; MEM, minimum essential medium; NEAA, non-essential amino acids; PNP, *p*-nitrophenol; CT, computed tomography; EDTA, ethylene diamine tetraacetic acid; SD, standard deviation; MPN, metal polyphenol network; EPS, extracellular polymeric substances; WBC, white blood cell; MON, monocyte; NEU, neutrophil; HE, hematoxylin-eosin; MBC, minimum bactericidal concentration; DLE, drug loading efficiency; DLC, drug loading capacity.

Data Sharing Statement

Data of this study will be made available upon reasonable request from the corresponding author.

Ethics Approval and Informed Consent

All experimental protocols in this study were approved by the Ethics Committee of Anhui Medical University (LLSC20231459). Animal housing and procedures were performed in accordance with the "Guiding Principles for the Care and Use of Animals" (China).

Consent for Publication

The author confirms:

that the work described has not been published before;

that it is not under consideration for publication elsewhere;

that its publication has been approved by all co-authors, if any;

that its publication has been approved (tacitly or explicitly) by the responsible authorities at the institution where the work carried out.

Acknowledgments

The authors thank the Center for Scientific Research of Anhui Medical University for valuable help in our experiment (Using a laser confocal scanning microscope to capture some of the immunofluorescence staining images. Using TEM and FE-SEM to capture some of the microstructure and size of Van@CuTA nanospheres and biofilms images.

Author Contributions

All authors made a significant contribution to the work reported, whether that is in the conception, study design, execution, acquisition of data, analysis and interpretation, or in all these areas; took part in drafting, revising or critically reviewing the article; gave final approval of the version to be published; have agreed on the journal to which the article has been submitted; and agree to be accountable for all aspects of the work.

Funding

This work was supported by Research fund of Anhui Translational Medicine Research Institute (2023zhyx-C60), Anhui province University Research project (2022AH051188, 2024AH010114), the Natural Science Foundation of Anhui Province (2308085MH248) and Anhui Province Clinical Medical Research Transformation Special Project (202304295107020043).

Disclosure

The authors declare that they have no known competing financial interests or personal relationships that could have influenced this work.

References

1. Kavanagh N, Ryan EJ, Widaa A, et al. Staphylococcal osteomyelitis: disease progression, treatment challenges, and future directions. *Clin Microbiol Rev.* 2018;31. doi: 10.1128/CMR.00084-17

2. Ren Y, Liu L, Sun D, et al. Epidemiological updates of post-traumatic related limb osteomyelitis in China: a 10 years multicentre cohort study. *Int J Surg*. 2023;109:2721–2731. doi:10.1097/JS9.0000000000000502
3. Lew DP, Waldvogel FA. Waldvogel F A Osteomyelitis. *Lancet*. 2004;364:369–379. doi:10.1016/S0140-6736(04)16727-5
4. Hamza HM, Malik MM, Asad M, et al. Advances in orthopedic implants: the role of nanotechnology in enhancing performance and longevity. *Regen Med Rep*. 2025;2:15–21. doi:10.4103/REGENMED.REGENMED-D-24-00024
5. Krauss JL, Roper PM, Ballard A, et al. Staphylococcus aureus infects osteoclasts and replicates intracellularly. *mBio*. 2019;10. doi: 10.1128/mBio.02447-19
6. Feng S, Yang Y, Liu Z, et al. Intracellular bacteriolysis contributes to pathogenicity of Staphylococcus aureus by exacerbating AIM2-mediated inflammation and necroptosis. *Virulence*. 2022;13:1684–1696. doi:10.1080/21505594.2022.2127209
7. Masters EA, Trombetta RP, de Mesy Bentley KL, et al. Evolving concepts in bone infection: redefining "biofilm", "acute vs. chronic osteomyelitis", "the immune proteome" and "local antibiotic therapy". *Bone Res*. 2019;7:20. doi:10.1038/s41413-019-0061-z
8. Lv H, Yang M, Yang Y, et al. Metal Ion and antibiotic co-loaded nanoparticles for combating methicillin-rresistant staphylococcus aureus-induced osteomyelitis. *ACS Nano*. 2025;19:5253–5268. doi:10.1021/acsnano.4c11956
9. Tong SYC, Fowler VG, Skalla L, et al. Management of Staphylococcus aureus bacteremia. *JAMA*. 2025;334:798–808. doi:10.1001/jama.2025.4288
10. Masters EA, Ricciardi BF, Bentley KLDM, Moriarty TF, Schwarz EM, Muthukrishnan G. Skeletal infections: microbial pathogenesis, immunity and clinical management. *Nat Rev Microbiol*. 2022;20:385–400. doi:10.1038/s41579-022-00686-0
11. Franzini M, Valdenassi L, Tirelli U, et al. Post-surgical wounds treated with ozone: a preliminary case series. *Med Gas Res*. 2024;14:225–227. doi:10.4103/mgr.MEDGASRES-D-23-00017
12. Namazoğlu B, Aksoy M, Memiş-özgül B, et al. Anti-microbial efficiency of gaseous ozone's combined use with fluoride and chlorhexidine on time-related oral biofilm: an in situ study on pediatric patients. *Med Gas Res*. 2023;13:192–197. doi:10.4103/2045-9912.372820
13. Willis JA, Cheburkanov V, Chen S, et al. Breaking down antibiotic resistance in methicillin-resistant Staphylococcus aureus: combining antimicrobial photodynamic and antibiotic treatments. *Proc Natl Acad Sci U S A*. 2022;119:e2208378119. doi:10.1073/pnas.2208378119
14. Zhang W, Lu H, Zhang W, et al. Inflammatory microenvironment-responsive hydrogels enclosed with quorum sensing inhibitor for treating post-traumatic osteomyelitis. *Adv Sci*. 2024;11:e2307969. doi:10.1002/advs.202307969
15. Lu G, Zhao G, Wang S, et al. Injectable nano-micro composites with anti-bacterial and osteogenic capabilities for minimally invasive treatment of osteomyelitis. *Adv Sci*. 2024;11:e2306964. doi:10.1002/advs.202306964
16. Liao S, Wu S, Mao C, et al. Electron aggregation and oxygen fixation reinforced microwave dynamic and thermal therapy for effective treatment of MRSA-induced osteomyelitis. *Small*. 2024;20:e2312280. doi:10.1002/smll.202312280
17. Jia B, Zhang Z, Zhuang Y, et al. High-strength biodegradable zinc alloy implants with antibacterial and osteogenic properties for the treatment of MRSA-induced rat osteomyelitis. *Biomaterials*. 2022;287:121663. doi:10.1016/j.biomaterials.2022.121663
18. Cheng Y, Zhang Y, Zhao Z, et al. Guanidinium-decorated nanostructure for precision sonodynamic-catalytic therapy of MRSA-infected osteomyelitis. *Adv Mater*. 2022;34:e2206646. doi:10.1002/adma.202206646
19. Zhang Y, Cheng Y, Zhao Z, et al. Enhanced chemoradiotherapy for MRSA-infected osteomyelitis using immunomodulatory polymer-reinforced nanotherapeutics. *Adv Mater*. 2024;36:e2304991. doi:10.1002/adma.202304991
20. Jin L, Liu X, Zheng Y, et al. Interfacial and defect polarization enhanced microwave noninvasive therapy for Staphylococcus aureus-infected chronic osteomyelitis. *ACS Nano*. 2023;17:18200–18216. doi:10.1021/acsnano.3c05130
21. Tsvetkov P, Coy S, Petrova B, et al. Copper induces cell death by targeting lipoylated TCA cycle proteins. *Science*. 2022;375:1254–1261. doi:10.1126/science.abf0529
22. Sun W, Wang C, Wan D, et al. CuCO bimetallic oxide rapidly treats Staphylococcus aureus-infected osteomyelitis through microwave strengthened microwave catalysis and fenton-therapy. *Small Methods*. 2023;7:e2300203. doi:10.1002/smtd.202300203
23. Li Y, Li J, Zhong Y, et al. pH-responsive and nanoenzyme-loaded artificial nanocells relieved osteomyelitis efficiently by synergistic chemodynamic and cuproptosis therapy. *Biomaterials*. 2025;313:122762. doi:10.1016/j.biomaterials.2024.122762
24. Karygianni L, Ren Z, Koo H, et al. Biofilm matrixome: extracellular components in structured microbial communities. *Trends Microbiol*. 2020;28:668–681. doi:10.1016/j.tim.2020.03.016
25. Mistry S, Roy R, Jha AK, et al. Treatment of long bone infection by a biodegradable bone cement releasing antibiotics in human. *J Control Release*. 2022;346:180–192. doi:10.1016/j.jconrel.2022.04.018
26. Hu Z, Shan J, Jin X, et al. Nanoarchitectonics of in situ antibiotic-releasing acicular nanozymes for targeting and inducing cuproptosis-like death to eliminate drug-resistant bacteria. *ACS Nano*. 2024;18:24327–24349. doi:10.1021/acsnano.4c06565
27. Mei J, Xu D, Wang L, et al. Biofilm microenvironment-responsive self-assembly nanoreactors for all-stage biofilm associated infection through bacterial cuproptosis-like death and macrophage re-rousing. *Adv Mater*. 2023;35:e2303432. doi:10.1002/adma.202303432
28. Sahiner N, Sagbas S, Sahiner M, et al. Biocompatible and biodegradable poly(Tannic Acid) hydrogel with antimicrobial and antioxidant properties. *Int J Biol Macromol*. 2016;82:150–159. doi:10.1016/j.ijbiomac.2015.10.057
29. Maghsoudi MAF, Aghdam RM, Asbagh RA, et al. 3D-printing of alginate/gelatin scaffold loading tannic acid@ZIF-8 for wound healing: in vitro and in vivo studies. *Int J Biol Macromol*. 2024;265:130744. doi:10.1016/j.ijbiomac.2024.130744
30. Akiyama H, Fujii K, Yamasaki O, et al. Antibacterial action of several tannins against Staphylococcus aureus. *J Antimicrob Chemother*. 2001;48:487–491. doi:10.1093/jac/48.4.487
31. Li J, Zhong W, Zhang K, et al. Biguanide-derived polymeric nanoparticles kill MRSA biofilm and suppress infection in vivo. *ACS Appl Mater Interfaces*. 2020;12:21231–21241. doi:10.1021/acsami.9b17747
32. Padzik M, Hendiger EB, Chomicz L, et al. Tannic acid-modified silver nanoparticles as a novel therapeutic agent against Acanthamoeba. *Parasitol Res*. 2018;117:3519–3525. doi:10.1007/s00436-018-6049-6
33. Li J, Li J, Wei J, et al. Copper tannic acid-coordinated metal-organic nanosheets for synergistic antimicrobial and antifouling coatings. *ACS Appl Mater Interfaces*. 2021;13:10446–10456. doi:10.1021/acsami.0c22321
34. Ke X, Tang S, Wang H, et al. Natural small biological molecule based supramolecular bioadhesives with innate photothermal antibacterial capability for nonpressing hemostasis and effective wound healing. *ACS Appl Mater Interfaces*. 2022;14:53546–53557. doi:10.1021/acsami.2c17415

35. Sun J, Zhu Y, Meng L, et al. Electrophoretic deposition of colloidal particles on Mg with cytocompatibility, antibacterial performance, and corrosion resistance. *Acta Biomater*. 2016;45:387–398. doi:10.1016/j.actbio.2016.09.007
36. Zhao Y, Li J, Liu L. Zinc-based tannin-modified composite microparticulate scaffolds with balanced antimicrobial activity and osteogenesis for infected bone defect repair. *Adv Healthc Mater*. 2023;12:e2300303. doi:10.1002/adhm.202300303
37. Fu M, Zhao Y, Wang Y, et al. On-demand removable self-healing and ph-responsive europium-releasing adhesive dressing enables inflammatory microenvironment modulation and angiogenesis for diabetic wound healing. *Small*. 2023;19:e2205489. doi:10.1002/smll.202205489
38. Orlowski P, Tomaszewska E, Ranoszek-Soliwoda K, et al. Tannic acid-modified silver and gold nanoparticles as novel stimulators of dendritic cells activation. *Front Immunol*. 2018;9:1115. doi:10.3389/fimmu.2018.01115
39. Lin S, Cheng Y, Zhang H, et al. Copper tannic acid coordination nanosheet: a potent nanozyme for scavenging ROS from cigarette smoke. *Small*. 2020;16:e1902123. doi:10.1002/smll.201902123
40. Shen Y, Xu Y, Yu Z, et al. Multifunctional injectable microspheres containing "naturally-derived" photothermal transducer for synergistic physical and chemical treating of acute osteomyelitis through sequential immunomodulation. *ACS Nano*. 2024. doi:10.1021/acsnano.3c10697
41. Pourshahrestani S, Unalan I, Zeimaran E, et al. Tannic acid-loaded zinc- and copper-doped mesoporous bioactive glass nanoparticles: potential antioxidant nanocarriers for wound healing. *Bioact Mater*. 2025;54:71–85. doi:10.1016/j.bioactmat.2025.07.046
42. Li D, Zhang C, Xiong Q, et al. Elongated magnetic nanorobots with multi-enzymatic cascades for active in vivo tumor targeting and enhanced chemodynamic therapy. *ACS Nano*. 2025;19:15040–15054. doi:10.1021/acsnano.5c01566
43. Xu J, Fang H, Zheng S, et al. A biological functional hybrid scaffold based on decellularized extracellular matrix/gelatin/chitosan with high biocompatibility and antibacterial activity for skin tissue engineering. *Int J Biol Macromol*. 2021;187:840–849. doi:10.1016/j.ijbiomac.2021.07.162
44. Xia W, Wu Z, Hou B, et al. Inactivation of antibiotic resistant bacteria by nitrogen-doped carbon quantum dots through spontaneous generation of intracellular and extracellular reactive oxygen species. *Mater Today Bio*. 2025;30:101428. doi:10.1016/j.mtbio.2024.101428
45. Song Y, Li H, Yuan Y, et al. Synergistic photothermal-sonodynamic therapy for antibacterial and immune reprogramming in chronic osteomyelitis. *J Control Release*. 2025;381:113612. doi:10.1016/j.jconrel.2025.113612
46. Hassani A, Khoshfetrat AB, Rahbarghazi R, et al. Collagen and nano-hydroxyapatite interactions in alginate-based microcapsule provide an appropriate osteogenic microenvironment for modular bone tissue formation. *Carbohydr Polym*. 2022;277:118807. doi:10.1016/j.carbpol.2021.118807
47. Li X, Zhang Q, Zhu Y, et al. Structural characterization of a mannoglucan polysaccharide from Dendrobium huoshanense and evaluation of its osteogenesis promotion activities. *Int J Biol Macromol*. 2022;211:441–449. doi:10.1016/j.ijbiomac.2022.05.036
48. Mullick P, Das G, Aiyagari R. Aiyagari R 2-Dodecylmalonic acid-mediated synthesis of mineralized hydroxyapatite amicable for bone cell growth on orthopaedic implant. *J Colloid Interface Sci*. 2022;608:2298–2309. doi:10.1016/j.jcis.2021.10.157
49. Jin Y, Liu H, Chu L, et al. Initial therapeutic evidence of a borosilicate bioactive glass (BSG) and Fe(3)O(4) magnetic nanoparticle scaffold on implant-associated Staphylococcal aureus bone infection. *Bioact Mater*. 2024;40:148–167. doi:10.1016/j.bioactmat.2024.05.040
50. Qiao Y, Wu S, Zheng Y, et al. Enhancing microwave dynamic effects via surface states of ultrasmall 2D MOF triggered by interface confinement for antibiotics-free therapy. *Adv Sci*. 2023;10:e2300084. doi:10.1002/advs.202300084
51. Radwan NH, Nasr M, Ishak RAH, et al. Chitosan-calcium phosphate composite scaffolds for control of post-operative osteomyelitis: fabrication, characterization, and in vitro-in vivo evaluation. *Carbohydr Polym*. 2020;244:116482. doi:10.1016/j.carbpol.2020.116482
52. Odekerken JC, Arts JJ, Surtel DA, et al. A rabbit osteomyelitis model for the longitudinal assessment of early post-operative implant infections. *J Orthop Surg Res*. 2013;8:38. doi:10.1186/1749-799X-8-38
53. Huang Y, Jiang C, Chen L, et al. Gli1 promotes the phenotypic transformation of valve interstitial cells through Hedgehog pathway activation exacerbating calcific aortic valve disease. *Int J Biol Sci*. 2023;19:2053–2066. doi:10.7150/ijbs.74123
54. Ghasemi S, Alibabaie A, Saberi R, et al. Evaluation of the effects of zein incorporation on physical, mechanical, and biological properties of polyhydroxybutyrate electrospun scaffold for bone tissue engineering applications. *Int J Biol Macromol*. 2023;253:126843. doi:10.1016/j.ijbiomac.2023.126843
55. Glaudemans A, Jutte PC, Cataldo MA, et al. Consensus document for the diagnosis of peripheral bone infection in adults: a joint paper by the EANM, EBJIS, and ESR (with ESCMID endorsement). *Eur J Nucl Med Mol Imaging*. 2019;46:957–970. doi:10.1007/s00259-019-4262-x
56. Wang J, Sheng Z, Liu Y, et al. Combined proteomic and transcriptomic analysis of the antimicrobial mechanism of tannic acid against Staphylococcus aureus. *Front Pharmacol*. 2023;14:1178177. doi:10.3389/fphar.2023.1178177
57. Zhang Y, Qi G, Qu X, et al. Smart tumor microenvironment-responsive nano-prodrug for disulfiram toxification in situ and the exploration of lethal mechanisms in cells. *Langmuir*. 2022;38:584–592. doi:10.1021/acs.langmuir.1c03256
58. Ha W, Yang JL, Shi YP. Antibacterial metal-phenolic nanosheets as smart carriers for the controlled release of epirubicin hydrochloride. *Nanoscale*. 2022;14:9806–9817. doi:10.1039/D2NR02066A
59. Liang Y, Wang W, Qi K, et al. Exudate Unidirectional Pump to Promote Glucose Catabolism Triggering Fenton-Like Reaction for Chronic Diabetic Wounds Therapy. *Adv Sci*. 2024;11:e2404652. doi:10.1002/advs.202404652
60. Liu M, Huang L, Xu X, et al. Copper doped carbon dots for addressing bacterial biofilm formation, wound infection, and tooth staining. *ACS Nano*. 2022;16:9479–9497. doi:10.1021/acsnano.2c02518
61. Zhang Q, Chen W, Li G, et al. A factor-free hydrogel with ROS scavenging and responsive degradation for enhanced diabetic bone healing. *Small*. 2024;20:e2306389. doi:10.1002/smll.202306389
62. Byun H, Jang GN, Hong MH, et al. Biomimetic anti-inflammatory and osteogenic nanoparticles self-assembled with mineral ions and tannic acid for tissue engineering. *Nano Converg*. 2022;9:47. doi:10.1186/s40580-022-00338-2
63. Sanchez CJ, Ward CL, Romano DR, et al. Staphylococcus aureus biofilms decrease osteoblast viability, inhibits osteogenic differentiation, and increases bone resorption in vitro. *BMC Musculoskelet Disord*. 2013;14:187. doi:10.1186/1471-2474-14-187
64. Shi C, Wu T, He Y, et al. Recent advances in bone-targeted therapy. *Pharmacol Ther*. 2020;207:107473. doi:10.1016/j.pharmthera.2020.107473
65. Wu S, Wu B, Liu Y, et al. Mini review therapeutic strategies targeting for biofilm and bone infections. *Front Microbiol*. 2022;13:936285. doi:10.3389/fmicb.2022.936285